

ARTICLE

<https://doi.org/10.1038/s41467-018-08257-9>

OPEN

Diverse manifestations of the mid-Pleistocene climate transition

Youbin Sun^{1,2}, Qiuzhen Yin³, Michel Crucifix³, Steven C. Clemens⁴, Pablo Araya-Melo³, Weiguo Liu^{1,2}, Xiaoke Qiang^{1,2}, Qingsong Liu⁵, Hui Zhao¹, Lianji Liang⁶, Hongyun Chen⁷, Ying Li¹, Li Zhang^{1,8}, Guocheng Dong^{1,8}, Ming Li¹, Weijian Zhou^{1,2,9}, Andre Berger³ & Zhisheng An^{1,2,10}

The mid-Pleistocene transition (MPT) is widely recognized as a shift in paleoclimatic periodicity from 41- to 100-kyr cycles, which largely reflects integrated changes in global ice volume, sea level, and ocean temperature from the marine realm. However, much less is known about monsoon-induced terrestrial vegetation change across the MPT. Here, on the basis of a 1.7-million-year $\delta^{13}\text{C}$ record of loess carbonates from the Chinese Loess Plateau, we document a unique MPT reflecting terrestrial vegetation changes from a dominant 23-kyr periodicity before 1.2 Ma to combined 100, 41, and 23-kyr cycles after 0.7 Ma, very different from the conventional MPT characteristics. Model simulations further reveal that the MPT transition likely reflects decreased sensitivity of monsoonal hydroclimate to insolation forcing as the Northern Hemisphere became increasingly glaciated through the MPT. Our proxy-model comparison suggests varied responses of temperature and precipitation to astronomical forcing under different ice/ CO_2 boundary conditions, which greatly improves our understanding of monsoon variability and dynamics from the natural past to the anthropogenic future.

¹ State Key Laboratory of Loess and Quaternary Geology, Institute of Earth Environment, Chinese Academy of Sciences, 710061 Xian, China. ² CAS Center for Excellence in Quaternary Science and Global Change, Chinese Academy of Sciences, 710061 Xian, China. ³ Georges Lemaître Center for Earth and Climate Research, Earth and Life Institute, Université Catholique de Louvain, 1348 Louvain-la-Neuve, Belgium. ⁴ Department of Earth, Environmental and Planetary Sciences, Brown University, Providence 02912-1846 RI, USA. ⁵ Centre for Marine Magnetism, Department of Ocean Science and Engineering, Southern University of Science and Technology, 518055 Shenzhen, China. ⁶ College of Architecture and Civil Engineering, Beijing University of Technology, 100022 Beijing, China. ⁷ The Institute of Hydrogeology and Environmental Geology, Chinese Academy of Geological Sciences, 050061 Shijiazhuang, China. ⁸ Shaanxi Key Laboratory of Accelerator Mass Spectrometry Technology and Application, 710061 Xian, China. ⁹ Interdisciplinary Research Center of Earth Science Frontier, Beijing Normal University, 100875 Beijing, China. ¹⁰ Open Studio for Oceanic-Continental Climate and Environment Changes, Pilot National Laboratory for Marine Science and Technology (Qingdao), 266200 Qingdao, China. Correspondence and requests for materials should be addressed to Y.S. (email: sunyb@ieecas.cn)

The Pleistocene climate is characterized by significant glacial–interglacial changes in high-latitude ice volume^{1–3}, global ocean temperature⁴, sea level⁵, and monsoonal climate⁶. All these variables inherently interacted to generate a remarkable transition of the ice-age cycles from 41-kyr to 100-kyr cycles between 1.2 and 0.7 Ma, called the mid-Pleistocene transition (MPT)^{2,7,8}. The MPT might be triggered by a nonlinear response to astronomical forcing⁹ induced by a secular CO₂ decrease and/or progressive regolith erosion^{10–12}. This transition is particularly apparent in numerous proxy indicators that are sensitive to changing glacial boundary conditions^{3–6,11,13}. At middle and low latitudes, however, the proxies of monsoon-induced wind and hydroclimate changes in the Arabian Sea and East Asia display prominent precession cycles during the middle-to-late Pleistocene^{14,15}.

Simulations with different climate models show that global monsoon changes are sensitive to changes in insolation, CO₂ concentration, and ice volume^{16–19}. Synthesis of Chinese loess, paleolake, and speleothem records confirms that the Asian summer monsoon variation was induced by combined effects of astronomical, ice, and CO₂ forcing²⁰. However, the relative roles of the insolation and coupled ice/CO₂ changes in driving orbital-scale monsoon variability remain controversial due to the spatial divergence and complexity of the proxy sensitivity to precipitation and temperature changes^{14,15,19–22}.

Here we present a centennial-resolution $\delta^{13}\text{C}$ record of inorganic carbonate ($\delta^{13}\text{C}_{\text{IC}}$) of a thick loess sequence from the northwestern Chinese Loess Plateau (CLP), a region sensitive to orbital-to-millennial-scale monsoon variability^{22,23}. Magnetostratigraphy and pedostratigraphy, together with burial dating, provide a reliable chronology of the loess–paleosol sequences accumulated over the past ~1.7 Ma. Loess $\delta^{13}\text{C}_{\text{IC}}$, a sensitive monsoon proxy, offers novel insights into Pleistocene monsoon variability and dynamics. Unlike the conventional expression of the MPT, our results reveal a compelling transition of the dominant rhythm in coupled monsoon–vegetation system from 23-kyr to combined 23-, 41-, and 100-kyr cycles across the MPT.

Results

Setting and sampling. CLP climate is characterized by seasonal changes in temperature and precipitation. Summer is the warm and humid season due to the influence of the summer monsoon, which transports heat and water vapor from the low-latitude oceans. The summer precipitation from May to September contributes to the annual precipitation by 60–75% and results in strong pedogenesis of the loess–paleosol sequences. In contrast, winter is the cold and dry season associated with strong winter monsoon wind, which is linked to the Siberian–Mongolian high-pressure system. The winter monsoon transports vast of dust particles from inland Asia to the downwind CLP. Therefore, Chinese loess, as a unique continental archive, can document multi-scale monsoon variability linked to past climate changes in both high- and low-latitude regions^{20–26}.

The Jingyuan loess sequence (JY, 36.35°N, 104.6°E, 2,210 m above sea level) is located at the depositional center of modern dust storms on the northwestern CLP (Fig. 1). A 430-m core was retrieved from the highest terrace of the Yellow River near Jingyuan County. The JY core consists of a 427-m loess deposit underlain by a 3-m gravel layer. A 40-m outcrop was excavated nearby to collect parallel samples spanning the last interglacial–glacial cycle. Continuous U-channel and discrete cube samples were taken from the split cores for alternating-field and thermal demagnetization measurements, respectively (Methods). Three quartz samples were chosen from the underlying gravel layer for ²⁶Al/¹⁰Be burial dating (Supplementary Fig. 1). Powder samples were taken at 10-cm intervals for magnetic susceptibility, grain size, and $\delta^{13}\text{C}_{\text{IC}}$ analyses.

Magnetostratigraphy and pedostratigraphy. Magnetic measurements and demagnetization spectra indicate that the JY loess sediments contain dominantly coarse-grained domain magnetite, which records the primary detrital remanent magnetization (Supplementary Figs. 2 and 3). Paleomagnetic results reveal that the Brunhes/Matuyama (B/M) boundary is recorded at the S₇/L₈ boundary and the Jaramillo subchron is located within S₁₀–L₁₃

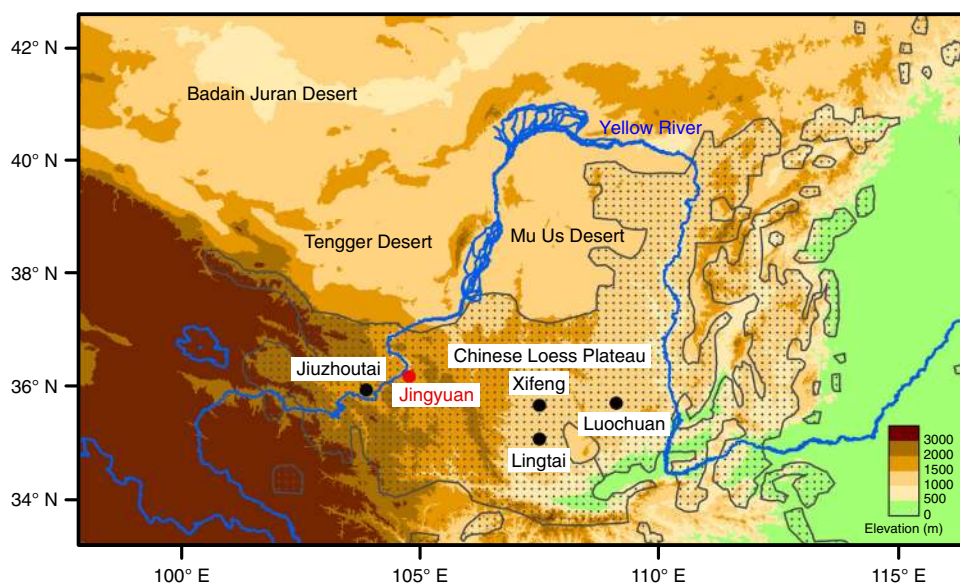


Fig. 1 Location of JY loess core and representative loess profiles on the Chinese Loess Plateau (CLP). Black dots denote four classic loess profiles, which have been investigated intensively as the Quaternary stratotype sections^{25–31}. Red dot indicates the Jingyuan loess profile accumulated on the ninth terrace of the Yellow River in the northwestern CLP^{23,41}

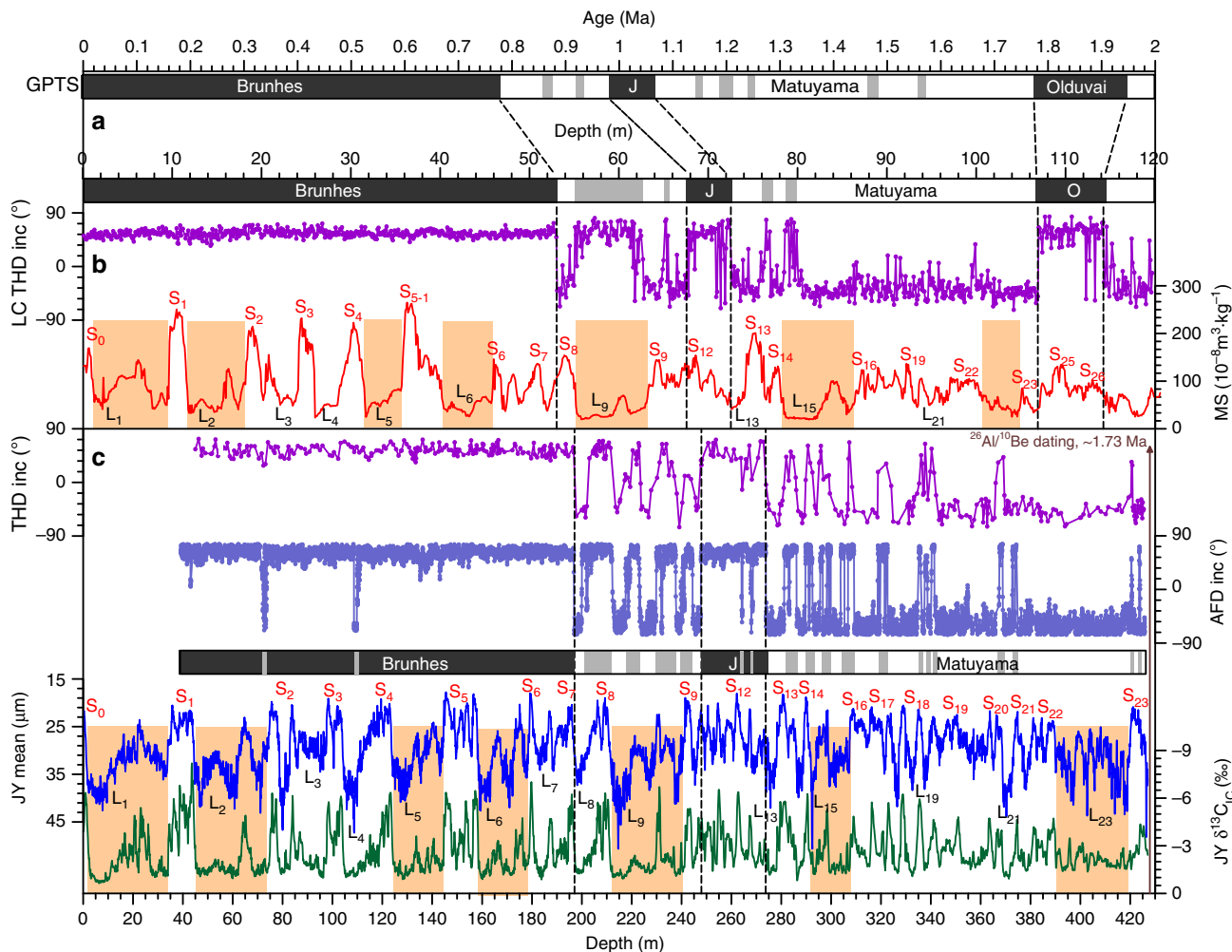


Fig. 2 Polarity and proxy variations of the JY loess sequence. **a** Geomagnetic polarity timescale (GPTS)^{32,33}. **b** Magnetic susceptibility (MS) and magnetostratigraphy of Luochuan (LC) profile^{27,31}. **c** JY $\delta^{13}C_{IC}$, mean, and magnetostratigraphy. The magnetostratigraphy is derived from inclination results measured by the alternating-field (AFD, light blue) and thermal (THD, purple) demagnetization methods. Dashed lines indicate the positions of paleomagnetic reversals (B/M Brunhes/Matuyama boundary, J Jaramillo, O Olduvai). Orange bars denote thick loess marker layers

(Fig. 2). The magnetostratigraphy of the JY loess sequence is well correlated with that of classic loess profiles from the central CLP^{27–31}, e.g., the B/M boundary at the top L_8 and the Jaramillo subchron between S_{10} and L_{13} (Supplementary Fig. 4). Correlation of the JY magnetostratigraphy with geomagnetic polarity timescale³² indicates that the Olduvai subchron is not recorded at the JY section (Fig. 2).

In addition, several normal excursions are evident in the inclination results below the B/M boundary, which either resulted from remagnetization of coarse-grained magnetic particles or are related to genuine geomagnetic excursions^{33,34}. Previous studies have deliberately evaluated the fidelity of these relatively short-lived directional anomalies, which could indicate remagnetization caused by physical realignment of magnetic grains in wetter conditions³⁵ or by viscous remanent magnetization overprinting on the coarse-grained eolian magnetic particles³⁶. The general correspondences between these short-lived directional anomalies and the grain-size curve seems supporting the remagnetization mechanism.

Loess–paleosol alternations can be reliably recognized and correlated throughout the entire CLP using magnetic susceptibility and grain-size variations. While the pedogenesis inferred from the magnetic susceptibility is relatively weak at the JY loess sequence, mean grain-size and $\delta^{13}C_{IC}$ variations faithfully

document the loess–paleosol alternations from S_{23} to S_0 (Fig. 2), consistent with the pedostratigraphy of other typical Chinese loess profiles^{25–31} (Supplementary Fig. 4). Seven thick loess units (L_1 , L_2 , L_5 , L_6 , L_9 , L_{15} , and L_{23}) can be readily identified as marker layers for pedostratigraphic correlation. In between these marker layers, JY loess–paleosol alternations from S_{23} to S_0 can be easily counted from the mean grain-size variations, which are quite similar to large-amplitude grain-size fluctuations of other representative loess profiles (Supplementary Fig. 4).

²⁶Al/¹⁰Be burial dating. The concentrations of ²⁶Al and ¹⁰Be in quartz were derived from the measured isotopic ratios (Methods). ¹⁰Be value was adjusted to match the currently accepted value³⁷, and the ²⁶Al/²⁷Al ratio was normalized to standards³⁸. For the Jingyuan location (latitude 36.35°N and elevation 2210 m)³⁹, cosmogenic nuclide production rates were estimated to be 150.42 and 22.09 atoms per gram per year for ²⁶Al and ¹⁰Be, respectively. Burial ages were calculated by iteratively solving equations without considering the post-burial cosmogenic nuclide production⁴⁰. Burial ages of three samples from the same gravel layer vary from 1.62 to 1.87 Ma, with uncertainties of 0.14–0.47 Ma (Table 1). The average age of basal gravel layer was estimated to be 1.73 ± 0.13 Ma, which is consistent with the timing of Lanzhou

loess sequence on the ninth terrace of the Yellow River⁴¹. Integrating the paleomagnetic results and the burial dates suggests that the JY loess sequence accumulated after 1.77 Ma.

Chronology. The loess chronology has been generated using both orbital tuning^{25,26} and a grain-size model^{24,42,43}. These approaches result in almost identical ages of the loess/paleosol boundaries from S_8 to S_0 , matching well with the timing of the glacial/interglacial transitions of benthic $\delta^{18}O$ stack³. During early-to-middle Pleistocene, orbital tuning can provide better constraints on the timing of the loess/paleosol boundaries compared to the grain-size age model approach due to the capacity for more time control points^{25,26}. However, orbital tuning can involve obliquity and precession imprints in the age model and thus hamper our assessment of the periodicity changes across the MPPT.

Owing to the strong similarity of loess–paleosol alternations between the Jingyuan core and other classic loess profiles, a pedostratigraphic age model can be developed using only 12 tie points to match 7 thick loess layers to the stacked grain-size time series^{25,26} (Fig. 3). The age model was refined by interpolation between 12 time controls using the weighted grain-size model²⁴. The basal age of the JY loess was estimated to be ~ 1.73 Ma, and

the sedimentation rate varies between 10 and 70 cm/kyr. The age model can be verified by a robust correlation of the Jingyuan grain-size variation with stacked loess grain-size^{25,26} and benthic $\delta^{18}O$ records³ (Fig. 3).

Reliability of this age model can be further assessed from the raw depth spectra over three depth intervals (Fig. 4a). The cyclicity ratios (27 m/11.5 m = 2.3 and 11.5 m/5.5 m = 2.1) in the depth spectra are consistent with the orbital ratios (100 kyr/41 kyr = 2.4 and 41 kyr/21 kyr = 2.0). Notably, a 5.5-m cycle is evident throughout the entire sequence and becomes dominant below L_{15} . Applying a 5.5 m = 21 kyr relationship results in a pedostratigraphic correlation of the lower portion to L_{15} – S_{23} and a basal age of ~ 1.73 Ma. Based on a linear depth–time transformation, an intrinsic cyclicity shift is evident from 23-kyr below L_{15} (1.2–1.7 Ma) to 100-kyr above L_9 (0–0.9 Ma) (Fig. 4b).

Alternatively, applying a 5.5 m = 41 kyr relationship could result in a pedostratigraphic correlation of the lower portion to L_{15} – S_{29} and a classic MPPT from 41- to 100-kyr cycles (Methods and Supplementary Fig. 5). This would require significantly lower sedimentation rate below L_{15} (13.5 cm/kyr) relative to that of the upper portion (25 cm/kyr above L_{15}). Such a remarkable change in the sedimentation rate below and above L_{15} is inconsistent with linear age–depth relationships of classic loess profiles on the CLP (Supplementary Fig. 6). Moreover, the basal age (~ 2.2 Ma) estimated from the alternative pedostratigraphic correlation is significantly older than independent paleomagnetic and burial dating results. Thus we consider that the alternative pedostratigraphic correlation is sedimentologically implausible.

Loess $\delta^{13}C_{IC}$ implication. Proxies related to vegetation change such as carbon isotopes of organic matter and inorganic carbonate in Chinese loess have been employed to assess coupled

Sample	^{26}Al (10^5 atoms/g)	^{10}Be (10^5 atoms/g)	$^{26}Al/^{10}Be$	Burial age (Ma)
JY-1 (sand)	3.17 ± 0.38	1.02 ± 0.17	3.10 ± 0.63	1.62 ± 0.47
JY-2 (gravel)	4.35 ± 0.24	1.45 ± 0.05	2.99 ± 0.19	1.69 ± 0.14
JY-3 (sand)	2.43 ± 0.41	0.88 ± 0.04	2.76 ± 0.48	1.87 ± 0.40
Average age				1.73 ± 0.13

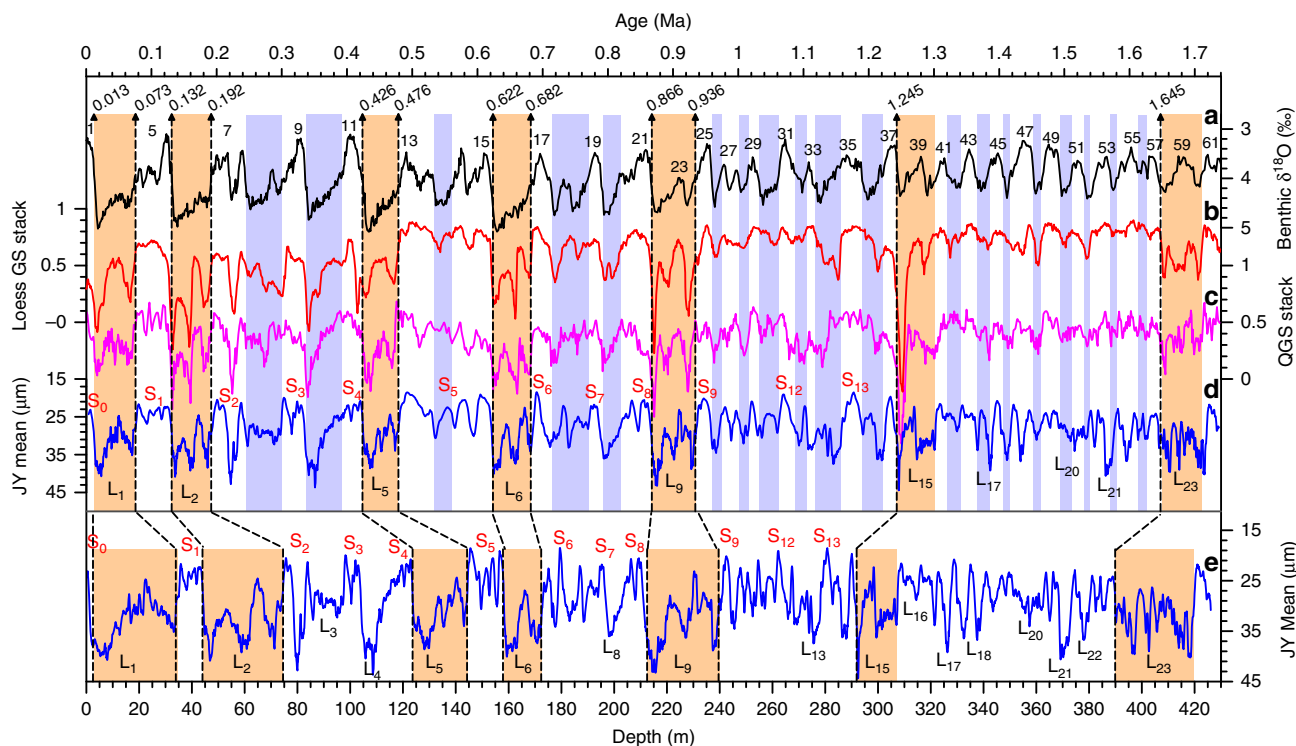


Fig. 3 Comparison of JY grain-size time series with stacked loess grain-size and benthic $\delta^{18}O$. **a** Benthic $\delta^{18}O$ stack³. **b** Loess grain-size (GS) stack²⁵. **c** Quartz grain-size (QGS) stack²⁶. **d** JY mean grain-size on age scale. **e** JY mean grain-size on depth scale. Dashed lines denote that the chronology was generated by matching the timing of seven loess marker layers (L_1 , L_2 , L_5 , L_6 , L_9 , L_{15} , and L_{23}) to stacked grain-size time series. Orange and blue bars indicated the correlation of thick marker layers and other loess units to glacial stages

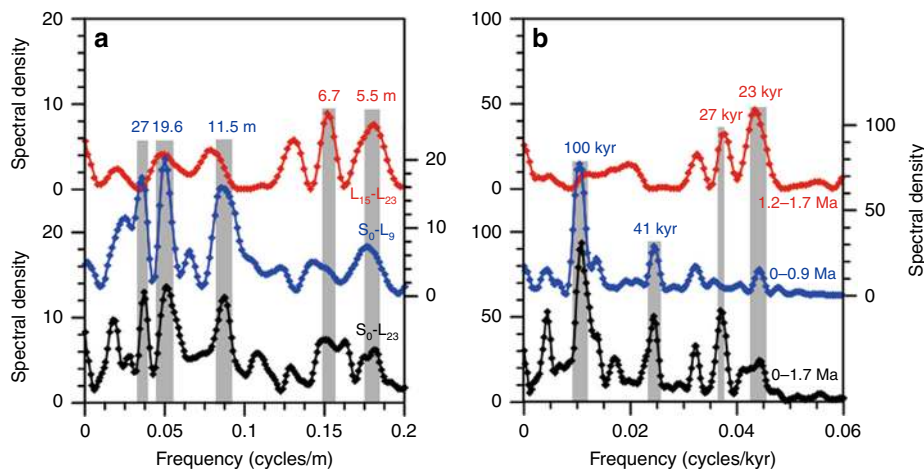


Fig. 4 Spectral results of JY $\delta^{13}\text{C}_{\text{IC}}$ record. **a** On depth scale, dominant cyclicity changes from 5.5 to 6.7 m/cycle below L_{15} to 19.6–27 m/cycle above L_9 . **b** The dominant cyclicity on age scale is evidently shifted from 23-kyr before 1.2 Ma (below L_{15}) to 100-kyr after 0.9 Ma (above L_9)

monsoon–vegetation changes^{44–47}. Both detrital and pedogenic carbonates are present in the Chinese loess deposits^{48,49}. Carbon isotopes of the detrital carbonates from dust source areas over inland Asia vary between a narrow range of -0.9% to 0.7% ²². Thus the carbon isotope of inorganic carbonate ($\delta^{13}\text{C}_{\text{IC}}$) in Chinese loess is controlled mainly by two factors: carbon isotopes of pedogenic carbonate and the proportion of pedogenic carbonates^{22,50}. The vegetation in the western CLP is dominated by C3 plants and its carbon isotopes varied by $\sim 2\text{--}3\%$ due to the biomass changes at glacial–interglacial timescales^{44,51,52}. The carbon isotopic difference between inorganic carbonate and organic matter indicates that secondary carbonates roughly contribute two thirds of the glacial–interglacial $\delta^{13}\text{C}_{\text{IC}}$ fluctuations ($\sim 7\%$), which is also attributed to changing vegetation density^{22,44}.

To determine the climate–vegetation linkage, the $\delta^{13}\text{C}_{\text{IC}}$ results of 20 surface soil samples over the CLP were compared with the precipitation and temperature data over 1981–2010 from the China meteorological data center (Supplementary Fig. 7). The correlation between the $\delta^{13}\text{C}_{\text{IC}}$ results and mean annual/summer precipitation is quite similar, whereas its correlation with the mean annual temperature is much higher than the mean summer temperature. Correlations between the $\delta^{13}\text{C}_{\text{IC}}$ of surface soil samples and climate variables reveal that while both mean annual temperature and precipitation can affect vegetation growth, mean annual summer precipitation likely plays a dominant role in the vegetation growth over the northwestern CLP. Since temperature and precipitation are strongly coupled over the CLP (i.e., warm–humid in summer and cold–dry in winter), loess $\delta^{13}\text{C}_{\text{IC}}$ can serve as a sensitive indicator of the monsoon-induced vegetation change during the Pleistocene.

The $\delta^{13}\text{C}_{\text{IC}}$ records display clear precession and millennial oscillations over the last 140 ka (Fig. 5), identical to those in Chinese speleothem and Greenland ice-core records^{15,53}. During marine isotope stage 5 (MIS 5), three negative peaks in the loess $\delta^{13}\text{C}_{\text{IC}}$ exhibit a decreasing trend from MIS 5e to MIS 5a, corresponding to changing summer insolation maxima. Our $\delta^{13}\text{C}_{\text{IC}}$ records also exhibit stadial–interstadial oscillations. Thirteen Heinrich-like events revealed by the loess $\delta^{13}\text{C}_{\text{IC}}$ records match well with weak summer monsoon intervals in the speleothem $\delta^{18}\text{O}$ and cold stadials in the Greenland ice core. High similarity between precession-to-millennial variability in Chinese loess, speleothem, and Greenland ice-core records confirms that our loess $\delta^{13}\text{C}_{\text{IC}}$ record is sensitive to both high-latitude temperature and low-latitude hydrological changes.

Sensitivity simulations. To estimate the monsoon sensitivity to various forcings, we use the set of 61 experiments with the climate model HadCM3⁵⁴, which were designed to sample the ensemble of glacial, CO_2 , and astronomical conditions experienced by the land–ocean–atmosphere system during the Pleistocene (Methods). A statistical model (called emulator) is used to interpolate the output of these experiments and to simulate the trajectory of the climate system throughout the Pleistocene. The model results are used to estimate the relative influences of different astronomical parameters (eccentricity, obliquity, and precession)³⁵, CO_2 concentrations (180–280 ppmv)^{56,57}, and discrete levels of glaciation ranging from 1 (Holocene-like) to 11 (Last Glacial Maximum)⁵⁴ (Supplementary Fig. 8).

As the loess $\delta^{13}\text{C}_{\text{IC}}$ record is affected by changes in mean annual precipitation (MAP) and temperature (MAT), we focused on these two variables averaged over northern China ($30\text{--}40^\circ\text{N}$, $104\text{--}120^\circ\text{E}$), where the precipitation change is more sensitive to summer monsoon intensity¹⁹. The sensitivity analysis was based on the emulator approach⁵⁴. The emulator is evaluated using a leave-one-out cross-validation approach, which consists of predicting the output of one experiment using the emulator calibrated on all the other experiments. Prediction errors for the MAT and MAP over northern China are well calibrated, and about 2/3 of the prediction errors are within one standard deviation (Supplementary Fig. 9).

The calibrated emulator is then used for two purposes. First, we estimated the evolution of these indices throughout the Pleistocene to reconstruct the MAP and MAT curves. The MAP and MAT values are the estimated equilibrium response of HadCM3 for forcing conditions spanning the last 1.7 Ma. The climate evolution estimated following this approach considers thus that MAT and MPT are in quasi-equilibrium with the forcing components, including astronomical solutions⁵⁵, ice levels³, and CO_2 concentrations^{56,57}. Next, we estimated the total variances of both MPT and MAT with the emulator, before and after the MPT. The expected variances of these variables caused by the variations of only one or two factors (eccentricity and longitude of perihelion, obliquity, ice, and CO_2) were estimated by assuming that the other factors are fixed⁵⁴.

Mid-Pleistocene monsoon transition. The mean grain-size (an indicator of the winter monsoon intensity^{25,26}) and $\delta^{13}\text{C}_{\text{IC}}$ (a proxy of monsoon-induced vegetation density^{22,44}) records display remarkable changes in both frequency and amplitude

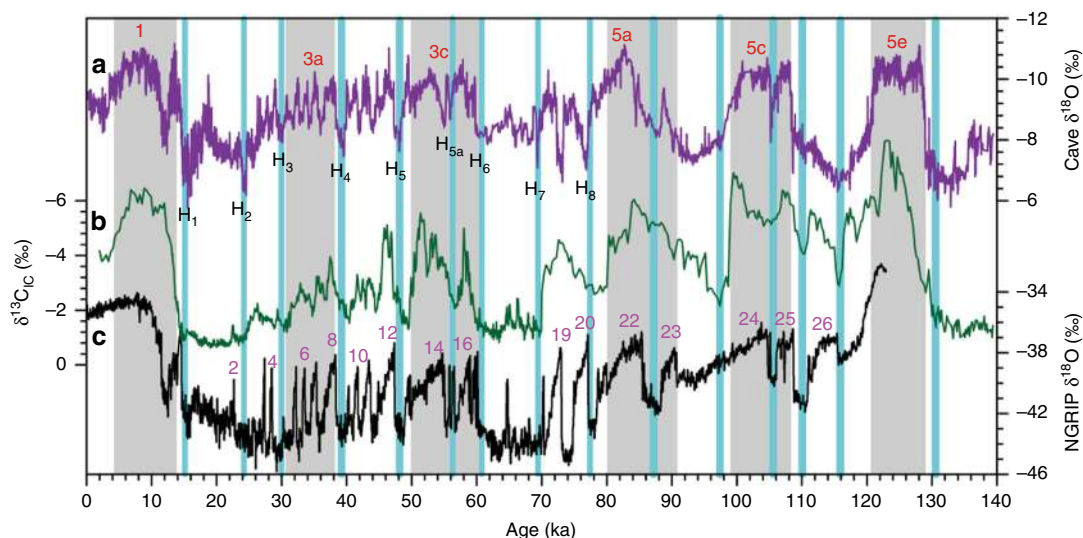


Fig. 5 Proxy variations over the last 140 ka from Greenland ice core, Chinese loess, and speleothem. **a** Chinese speleothem $\delta^{18}\text{O}$ record¹⁵. **b** JY loess $\delta^{13}\text{C}_{\text{IC}}$. **c** Greenland ice-core $\delta^{18}\text{O}$ record⁵³. Dashed lines denote correlations of positive loess $\delta^{13}\text{C}_{\text{IC}}$ and speleothem $\delta^{18}\text{O}$ with low Greenland temperature

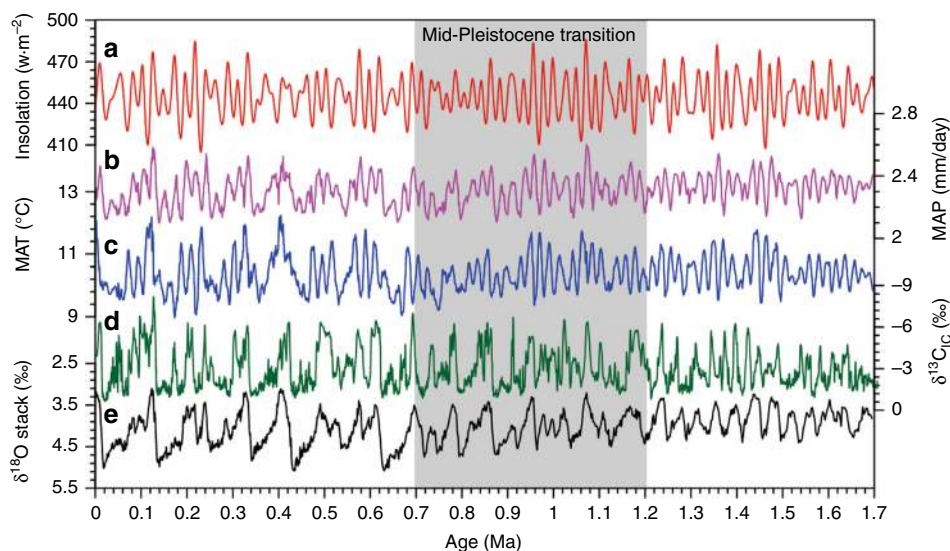


Fig. 6 Variations of proxy data and model results over the past 1.7 Ma. **a** Summer insolation at 65°N ⁵⁵. **b** Simulated mean annual precipitation (MAP) and **c** mean annual temperature (MAT) over the northern China. **d** JY loess $\delta^{13}\text{C}_{\text{IC}}$ record. **e** Benthic $\delta^{18}\text{O}$ stack³. The gray bar denotes the mid-Pleistocene transition

around two coarsening loess units (L_{15} and L_9) (Fig. 2). Notably, the $\delta^{13}\text{C}_{\text{IC}}$ records show a distinctive transition from rapid oscillations (5.5 and 6.7 m/cycle) below L_{15} to low-frequency fluctuations (11.5, 19.6 and 27 m/cycle) above L_9 , representing an intrinsic shift from 23-kyr before 1.2 Ma to 41- and 100-kyr cycles after 0.9 Ma (Fig. 4). Over longer timescales, the loess $\delta^{13}\text{C}_{\text{IC}}$ record exhibits distinctive glacial–interglacial and precessional variability over the past 1.7 Ma, which differs significantly from both summer insolation and benthic $\delta^{18}\text{O}$ (Fig. 6). In the loess $\delta^{13}\text{C}_{\text{IC}}$ records, precessional cycles were dominant before 1.2 Ma, followed by a mixing of 23- and 41-kyr cycles during the mid-Pleistocene. After 0.9 Ma, the 100-kyr glacial–interglacial cycles became dominant relative to the already present 41- and 23-kyr periodicities. The durations and rhythms of the interglacial climate varied significantly across the MPT. The past eight interglacials (MIS 21–1) are characterized by reduced precession-band variance and long

durations (30–60 kyr) compared to precession-dominated interglacials before the MPT.

The timing and duration of the MPT is well illustrated using continuous wavelet transforms (Methods and Fig. 7). Unlike the classical expression of a shift from 41- to 100-kyr cycles revealed by the benthic $\delta^{18}\text{O}$ stack, our loess $\delta^{13}\text{C}_{\text{IC}}$ records document a diverse shift of the dominant periodicity from 23- to 100-kyr cycles across the MPT. In the loess $\delta^{13}\text{C}_{\text{IC}}$ spectrum, the 23-kyr cycles were dominant before 1.2 Ma and weakened after 0.7 Ma, in contrast to the persistent precession cycles in the summer insolation spectrum. Meanwhile, the 100-kyr power initiated at 1.2 Ma and became dominant after 0.7 Ma. The benthic $\delta^{18}\text{O}$ spectrum, however, shows that the dominant periodicity shifted from 41-kyr cycles before 1.2 Ma to 100-kyr cycles after 0.7 Ma. While the timing and duration of the MPT are similar between terrestrial and marine records, different transitions in the frequency domain point to unique mechanisms governing the

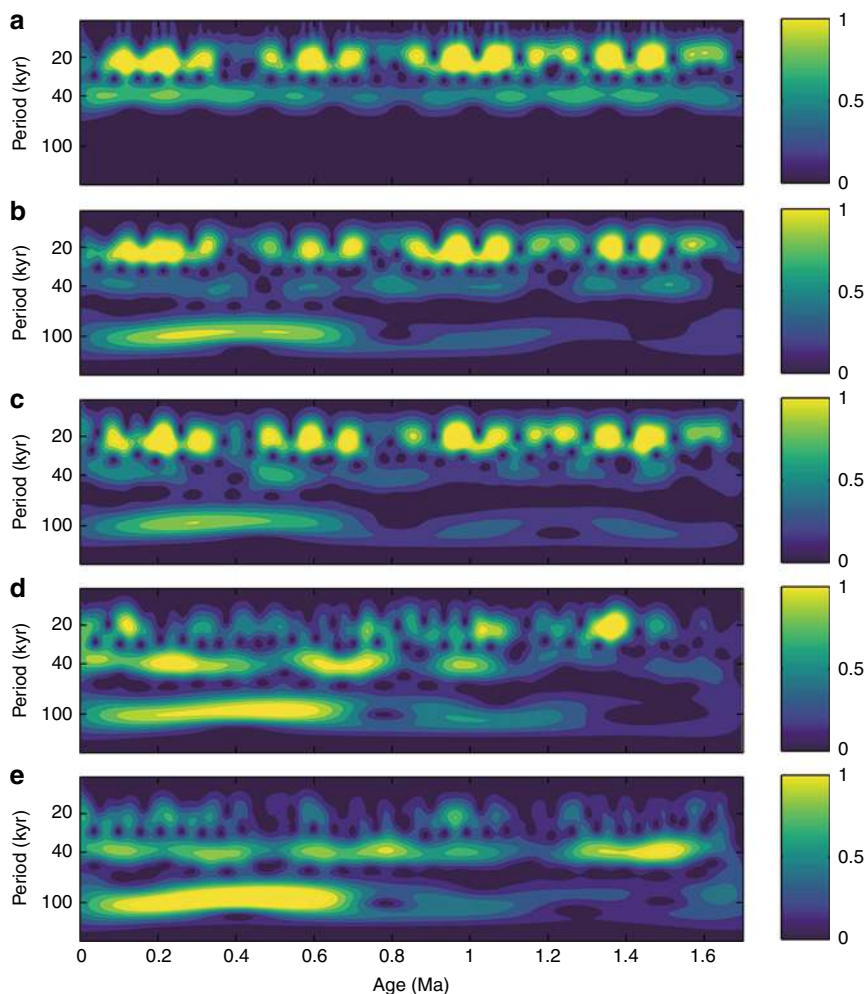


Fig. 7 Wavelet power spectra. **a** Summer insolation⁵⁵, **b** simulated MAP, **c** simulated mean annual temperature, **d** loess $\delta^{13}\text{C}_{\text{IC}}$, and **e** benthic $\delta^{18}\text{O}$ stack³

East Asian monsoon–vegetation responses to astronomical and coupled ice/ CO_2 forcing.

Discussion

Astronomical parameters and lower boundary configurations are key factors affecting orbital-scale monsoon variability^{16–19}. To test the plausible links of the monsoon–vegetation variability to changing insolation and ice sheets, we performed cross-wavelet analyses of the loess $\delta^{13}\text{C}_{\text{IC}}$ with summer insolation and the benthic $\delta^{18}\text{O}$. Cross-wavelet spectra reveal that over the Pleistocene the 23- and 41-kyr cycles in the $\delta^{13}\text{C}_{\text{IC}}$ records show strong coherence with the precession and obliquity signals, while remarkable glacial–interglacial fluctuations at both the 100- and 41-kyr periodicities started to be highly coupled with the benthic $\delta^{18}\text{O}$ stack after the MPT (Fig. 8). Different coherency of the loess $\delta^{13}\text{C}_{\text{IC}}$ with summer insolation and the benthic $\delta^{18}\text{O}$ mainly in the 100-kyr band suggests that evolving glacial boundary conditions across the MPT may have diminished the climate sensitivity to astronomical forcing by placing strong ice/ CO_2 constraints on the coupled monsoon–vegetation system.

The major differences of these forcing factors across the MPT are the ice extent and CO_2 concentration during glacial maxima^{3,58}. Thus sensitivity analyses were based on full glacial–interglacial ranges of the ice levels (1–11) and CO_2 concentrations (180–280 ppmv) after the MPT and half ranges of the ice levels (1–6) and CO_2 concentrations (220–280 ppmv) before

the MPT. Sensitivity results indicate that the MAT is primarily determined by both precession and CO_2 , and to a lesser extent by ice, and the MAP is mainly driven by precession and less by ice and CO_2 (Fig. 9). The coupled ice/ CO_2 impact on the MAT is largely attributed to the CO_2 change, whereas their impact on the MAP is a combination of both ice and CO_2 changes. Most remarkable differences across the MPT are the decreased sensitivities of both the MAP and MAT to precession forcing and the increased sensitivities of only the MAT to the CO_2 and coupled ice/ CO_2 forcing. MAT is thus less sensitive to precession forcing after the MPT when the Northern Hemisphere was more glaciated.

Different sensitivities of the MAP and MAT changes to precession, ice, and CO_2 forcing can lead to diverse manifestations in the amplitude and frequency domains across the MPT (Fig. 6). The simulated MAP over northern China during the last 1.7 Ma shows a persistent 23-kyr periodicity, while the ice/ CO_2 modulation on the MAP became distinctive during glacial periods after 0.9 Ma. By contrast, the simulated MAT change exhibits relatively warm interglacials during 1.5–0.9 Ma and an increase in glacial–interglacial amplitude after the mid-Brunhes event (~ 0.42 Ma)⁵⁹. Wavelet spectra of the simulated MAP and MAT reveal a distinctive transition from a dominant 23-kyr periodicity before 1.2 Ma to combined 23- and 100-kyr cycles after 0.7 Ma (Fig. 7). Filtered 100- and 23-kyr components in these proxies confirm that the onset of the 100-kyr cycle across the MPT is evident in the loess $\delta^{13}\text{C}_{\text{IC}}$, and simulated MAT and MAP, while the 23-kyr

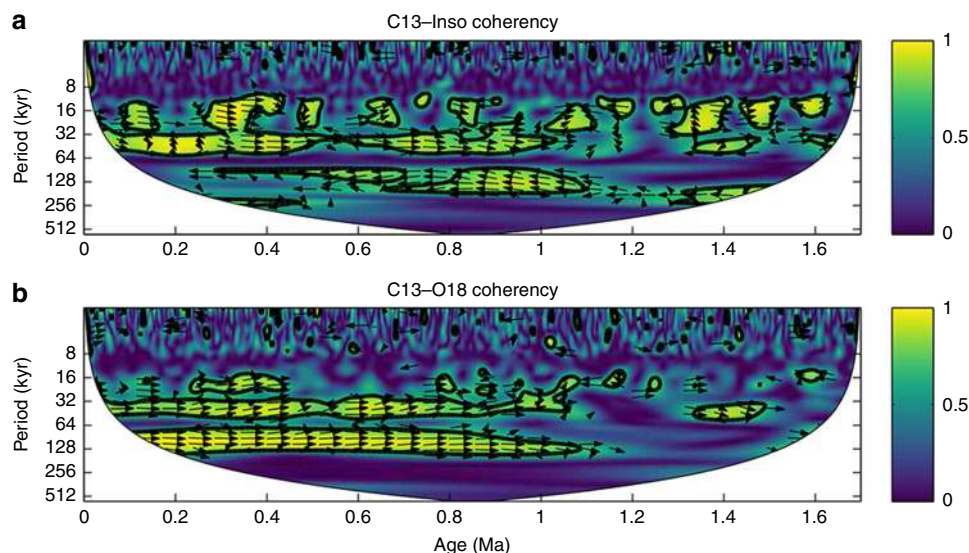


Fig. 8 Cross wavelet spectra. **a** JY loess $\delta^{13}\text{C}_{\text{IC}}$ vs. summer insolation⁵⁵, **b** JY loess $\delta^{13}\text{C}_{\text{IC}}$ vs. benthic $\delta^{18}\text{O}$ stack³. Black contours indicate the coherence above 5% significance level

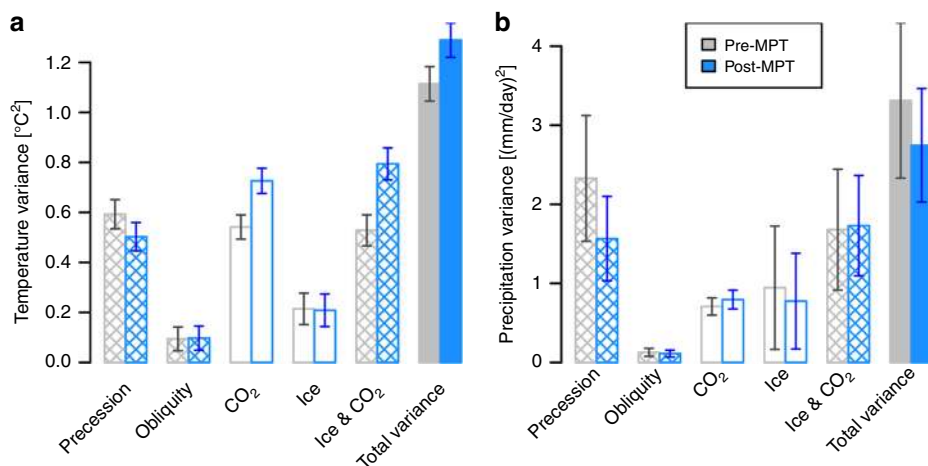


Fig. 9 Sensitivity of temperature and precipitation to astronomical, ice, and CO_2 forcing. **a** Mean annual temperature (MAT) and **b** mean annual precipitation (MAP) responses to precession and obliquity, ice, CO_2 , and coupled ice/ CO_2 forcing. Temperature and precipitation variances are spited into contributions for precession, obliquity, ice, CO_2 , and coupled ice and CO_2 variation before the MPT (pre-MPT, gray) and after the MPT (post-MPT, blue), respectively. The combined ice/ CO_2 contribution is not estimated by simply adding up the individual impacts of ice and CO_2 because their effects can partly cancel out each other

cycle is less evident in the benthic $\delta^{18}\text{O}$ than other three proxies (Supplementary Fig. 10). As the MAT and MAP are two important factors affecting the vegetation growth over the CLP, their frequency changes are imprinted in the $\delta^{13}\text{C}_{\text{IC}}$ record as a transition from the dominant 23-kyr to combined 23-, 41-, and 100-kyr cycles across the mid-Pleistocene.

In summary, our loess $\delta^{13}\text{C}_{\text{IC}}$ time series, for the first time, illustrate a transition of coupled monsoon–vegetation changes from a dominant 23-kyr periodicity to the combined 23-, 41-, and 100-kyr cycles during the mid-Pleistocene, differing from the well-known MPT from 41- to 100-kyr cycles in most marine-based proxy records. While the MPT was usually associated with an increase in ice volume denoted by addition of 41- and 100-kyr variances in the benthic $\delta^{18}\text{O}$ record, sensitivity experiments indicate that the ice impacts on the MAT and MAP over northern China did not vary significantly across the MPT. Rather, the large-amplitude 100-kyr cycle in loess $\delta^{13}\text{C}_{\text{IC}}$ is likely attributed to the amplified effect of glacial–interglacial CO_2

changes on the MAT. Proxy-model comparison reveals that the monsoon–vegetation changes responded dominantly to astronomical forcing before the MPT when the ice and CO_2 variability was relatively small. After the MPT, however, the precession forcing was attenuated by the coupled ice– CO_2 effects. Our results highlight varied roles of insolation and coupled ice/ CO_2 factors in driving the temperature and hydroclimate changes from the natural past to the anthropogenic future.

Methods

Drilling and sampling. In 2008, we drilled a 430-m core with a recovery rate of 98% at the highest tableland near Jingyuan County. The core consists of a 427-m loess deposits underlain by 3-m gravel layer. Since the recovery rate for the upper 40-m is <85%, we investigated a nearby 40-m outcrop to collect powder samples spanning the last interglacial–glacial cycle. Continuous U-channel samples were taken from the split core sections (40–427 m) for alternating-field magnetization (AFD) measurement. Discrete samples were also collected at 0.5-m intervals using nonmagnetic quartz tubes for thermal demagnetization (THD) measurement. An upcore orientation mark was scribed on the U-channel and tube samples to provide a vertical reference.

Magnetic measurements. Using a MFK1-FA Kappabridge equipped with a CS-3 high-temperature furnace, temperature-dependent susceptibility ($\kappa-T$) curves were measured in an argon atmosphere from room temperature up to 700 °C with a heating rate of 11 °C/min and then back to room temperature. Hysteresis loops and the first-order reversal curve diagrams were obtained using a MicroMag 3900 automated vibrating sample magnetometer in a maximum field of 1000 mT. Stepwise isothermal remanent magnetization acquisition and direct current demagnetization of saturation isothermal remanence was conducted on the same samples. Hysteresis parameters were calculated after subtracting paramagnetic contributions. A Day plot was used to estimate the domain state and grain size of the magnetic particles.

Stepwise thermal demagnetization was performed on the tube samples from room temperature up to 620–640 °C using a Thermal Demagnetizer (ASC TD-48). The U-channel samples were subjected to progressive AFD at peak fields up to 90 at 2.5–10-mT intervals. The natural remanence of the tube and U-channel samples was measured using a 2 G Enterprises Model 755 cryogenic magnetometer in a magnetically shielded room (<150 nT). Most samples exhibit a weak viscous overprint, which can be removed at the alternating field of 20 mT or at thermal treatment with temperature >300 °C. Principal component analysis, calculated with a least square linear fit, was performed on the demagnetization data. The characteristic remanent magnetization directions were determined by a least-square fitting of the THD results between 300 and 585 °C and of the AFD between 20 and 90 mT, with a maximum angular deviation <15°.

²⁶Al/¹⁰Be burial dating. Several kilograms of quartz-bearing sediments were collected from the gravel layer underlying the Jingyuan loess sequence. The quartzose sand and gravel samples were selected for crushing and then the 0.25–0.50-mm fractions were isolated for further purification. Carbonates were dissolved with HCl and magnetic minerals were removed using magnetic separation. The quartz fractions were then leached repeatedly in hot agitated 5% HF/HNO₃ overnight. The purified quartz fraction was dissolved in 5:1 HF/HNO₃ and spiked with ~0.3 mg ⁹Be. An aliquot was taken for determining the aluminum content using inductively coupled plasma–atomic emission spectrometry. After evaporation and fuming of the remaining solution in HClO₄, Al and Be were separated on ion-exchange columns in 0.4 M oxalic acid, precipitated as hydroxides, and transformed to oxides in a furnace at 900 °C. BeO was mixed with niobium and Al₂O₃ with copper powder for ¹⁰Be/⁹Be and ²⁶Al/²⁷Al measurement by accelerator mass spectrometer at Xi'an AMS Center, Institute of Earth Environment, Chinese Academy of Sciences.

An alternative age model. A different age model applied to the JY loess–paleosol sequence would generate a shift similar to the classic MPT from 41-kyr to 100-kyr cycles. In this case, the duration of the lower portion (below L₁₅) needs to be extended from 480 kyr (AGE1, 1.25–1.73 Ma) to 950 kyr (AGE2, 1.25–2.2 Ma) (Supplementary Fig. 5). On the AGE1 model, the lower portion of the JY loess core is correlated to L₁₅–S₂₃, whereas on the AGE2 model, this portion is correlated to L₁₅–S₂₉. We prefer the first age model (AGE1) because of two reasons. First, the Olduvai subchron is not recorded in the Jingyuan loess sequence and thus the basal age should be <1.77 Ma. Second, a remarkable shift of the sedimentation rate from 13.5 to 25 cm/kyr around L₁₅ based on the JY-AGE2 is significantly different from the relative stable sedimentation rates in several classic loess profiles since the Olduvai subchron (Supplementary Fig. 6). Such a two-fold increase of the sedimentation rate at this single site cannot be explained by either tectonic or climatic factors.

In addition, numerous geomorphologic and paleomagnetic investigations on the terrace sequences of the Yellow River indicate that the loess sequences (S₀–S₂₄) accumulated on the oldest terrace are <1.8 Ma^{28,41}. Based on the new terrace classification of the Yellow River⁴¹, Jingyuan loess sequences (S₀–S₂₃) was accumulated on the ninth terrace, with a rough basal age of 1.7 Ma. While an alternative pedostratigraphic correlation of the lower portion below L₁₅ can generate a classical MPT shift from 41-kyr to 100-kyr cycles, the relatively old basal age (~2.2 Ma) and two-fold increase in the sedimentation rates around L₁₅ are apparently inconsistent with independent dating results and with age–depth relationships of other classic loess profiles on the CLP, respectively. Thus we think that our preferred AGE1 is more reasonable, as inferred from the paleomagnetic and burial dating results.

Spectral and wavelet analyses. Spectral analysis was conducted using the Redfit 3.5 software⁶⁰. Wavelet analyses of loess $\delta^{13}\text{C}_{\text{IC}}$, simulated MAT and MAT, benthic $\delta^{18}\text{O}^3$, and summer insolation⁵⁵ were performed using MATLAB codes⁶¹ and a Morlet software package⁶². In order to visualize amplitude and frequency modulations, these data sets, except for the summer insolation, were preprocessed to isolate the 100-, 41-, and 21-kyr components using band-passing filters with central frequencies of 0.001, 0.025, and 0.05/kyr and bandwidths of 0.0002, 0.005, and 0.01/kyr before performing the wavelet transforms. The filtered signals are concentrated at three primary astronomical bands and then summed up for wavelet transforms. This preprocessing procedure can reduce the contribution of non-astronomical frequencies in the input signals and therefore improve the calculated power of three astronomical components in the paleoclimatic time series. Wavelet

transform coherence was analyzed to assess high-amplitude responses of the loess $\delta^{13}\text{C}_{\text{IC}}$, benthic $\delta^{18}\text{O}$ and summer insolation at three orbital bands.

Sensitivity experiments. We use 61 sensitivity experiments designed to sample efficiently changes in the astronomical configurations, CO₂ concentrations, and Northern Hemisphere glaciations experienced during the Pleistocene⁵⁴ (Supplementary Fig. 8). Each experiment is 300-year long and we retained averages over the last 100 years for subsequent analysis. The level of Northern Hemisphere glaciations is represented by one variable called “glaciation index,” and which refers to the 1 of the 11 stages of increasing glaciation sampled from the past glacial–interglacial cycle⁶³. Level 1 is the Holocene, and level 11 is the Last Glacial Maximum. We note that the configuration choice is such that ice extent grows mainly between stages 1 and 3, while ice thickness growth mainly between levels 3 and 11. Hence, by applying this design to represent ice volume changes during the early Pleistocene, we formulate the hypothesis that area fluctuations of ice sheets before the MPT were similar to after the MPT, but their thickness was smaller.

The sensitivity of the monsoon climate to the full spectrum of climatic conditions experienced during the Pleistocene is estimated using the climate model HadCM3⁶⁴. The atmospheric component dynamics are resolved on a 3.75° × 2.5° longitude–latitude grid, and the oceanic component has a horizontal resolution of 1.25° × 1.25°. The HadCM3 has been shown to capture well enough the monsoon–ENSO interaction⁶⁵ and natural variability of the summer rainfall over China⁶⁶. Compared to observations, the summer subtropical anticyclone in HadCM3 is too strong as in many other models. This circulation anomaly tends to induce much rainfall over the maritime continent, but the error in North China turns out to be very small (<1 mm/day) and thus quite acceptable for our purpose.

In order to generate a forcing–response scenario over the Pleistocene, we scaled the benthic $\delta^{18}\text{O}$ stack³ to estimate the glaciation index over the last 1.7 Myr. CO₂ concentration over the past 0.8 Ma is obtained from Antarctic records^{56,57}. The CO₂ before the 0.8 Ma was extrapolated to follow a linear relationship between ice volume and CO₂ concentrations over the past eight glacial cycles (Supplementary Fig. 8). The MAP and MAT values are the estimated equilibrium responses of HadCM3 for forcing conditions spanning the last 1.7 Ma by steps of 1 kyr. Validation for the MAT and MAP over northern China suggests that temperature is overall easier to predict than precipitation changes (Supplementary Fig. 9). Indeed, the annual precipitation response results from partly compensating trends in winter and summer. Annual changes are therefore smaller than seasonal changes and more difficult to detect over the internal model variability background. Error bars on the variances of the MAT and MAP correspond to the error variance of the emulator estimates. They combine internal model variability, which affects the values of the 100-year long averages used to calibrate the emulator. Uncertainty might come from the fact that we only have a limited number of experiments to map the sensitivity of HadCM3 to continuous changes in input variables.

Data availability

All relevant data that support the findings of this research are available from the corresponding author on request.

Received: 1 June 2018 Accepted: 20 December 2018

Published online: 21 January 2019

References

- Hays, J. D., Imbrie, J. & Shackleton, N. J. Variations in the Earth's orbit: pacemaker of the ice ages. *Science* **194**, 1121–1132 (1976).
- Ruddiman, W., Raymo, M., Martinson, D., Clement, B. & Backman, J. Pleistocene evolution: Northern Hemisphere ice sheets and North Atlantic Ocean. *Paleoceanography* **4**, 353–412 (1989).
- Lisiecki, L. & Raymo, M. A Pliocene–Pleistocene stack of 57 globally distributed benthic $\delta^{18}\text{O}$ records. *Paleoceanography* **20**, PA1003 (2005).
- Herbert, T. D., Peterson, L. C., Lawrence, K. & Liu, Z. H. Tropical Ocean temperatures over the past 3.5 million years. *Science* **328**, 1530–1534 (2010).
- Rohling, E. J. et al. Sea-level and deep-sea-temperature variability over the past 5.3 million years. *Nature* **508**, 477–482 (2014).
- deMenocal, P. B. Plio–Pleistocene African climate. *Science* **270**, 53–59 (1995).
- Pisias, N. G. Jr. & Moore, T. C. The evolution of the Pleistocene climate: a time series approach. *Earth Planet. Sci. Lett.* **52**, 450–458 (1981).
- Raymo, M. E., Oppo, D. W. & Curry, W. B. The mid-Pleistocene climate transition: a deep sea carbon perspective. *Paleoceanography* **12**, 546–559 (1997).
- Imbrie, J. et al. On the structure and origin of major glaciation cycles: 2. The 100,000 year cycle. *Paleoceanography* **8**, 699–735 (1993).
- Berger, A., Li, X. S. & Loutre, M. F. Modelling northern hemisphere ice volume over the last 3 Ma. *Quat. Sci. Rev.* **18**, 1–11 (1999).
- Clark, P. et al. The middle Pleistocene transition: characteristics, mechanisms, and implications for long-term changes in atmospheric pCO₂. *Quat. Sci. Rev.* **25**, 3150–3184 (2006).

12. Ganopolski, A. & Calov, R. The role of astronomical forcing, carbon dioxide and regolith in 100 kyr glacial cycles. *Clim. Past* **7**, 1415–1425 (2011).
13. Raymo, M. E., Lisiecki, L. E. & Nisancioglu, K. H. Plio-Pleistocene ice volume, Antarctic climate, and the global $\delta^{18}\text{O}$ record. *Science* **313**, 492–495 (2006).
14. Clemens, S. C., Prell, W. L. & Sun, Y. B. Astronomical-scale timing and mechanisms driving Late Pleistocene Indo-Asian Summer monsoons: reinterpreting cave speleothem $\delta^{18}\text{O}$. *Paleoceanography* **25**, PA4207 (2010).
15. Cheng, H. et al. The Asian monsoon over the past 640,000 years and ice age terminations. *Nature* **534**, 640–646 (2016).
16. Prell, W. L. & Kutzbach, J. E. Sensitivity of the Indian monsoon to forcing parameters and implications for its evolution. *Nature* **360**, 647–652 (1992).
17. deMenocal, P. B. & Rind, D. Sensitivity of Asian and African climate to variations in seasonal insolation, glacial ice cover, sea surface temperature, and Asian orography. *J. Geophys. Res.* **98**, 7265–7287 (1993).
18. Yin, Q. Z. & Berger, A. Individual contribution of insolation and CO_2 to the interglacial climates of the past 800,000 years. *Clim. Dyn.* **38**, 709–724 (2012).
19. Liu, Z. Y. et al. Chinese cave records and the East Asia summer monsoon. *Quat. Sci. Rev.* **83**, 115–128 (2014).
20. An, Z. S. et al. Global monsoon dynamics and climate change. *Annu. Rev. Earth Planet. Sci.* **43**, 2.1–2.49 (2015).
21. Clemens, S. C. et al. Precession-band variance missing from East Asian monsoon runoff. *Nat. Commun.* **9**, 3364 (2018).
22. Sun, Y. B. et al. Astronomical and glacial forcing of East Asian summer monsoon variability. *Quat. Sci. Rev.* **115**, 132–142 (2015).
23. Sun, Y. B. et al. Influence of Atlantic meridional overturning circulation on the East Asian winter monsoon. *Nat. Geosci.* **5**, 46–49 (2012).
24. Porter, S. C. & An, Z. S. Correlation between climate events in the North Atlantic and China during last glaciation. *Nature* **375**, 305–308 (1995).
25. Ding, Z. L. et al. Stacked 2.6-Ma grain size record from the Chinese loess based on five sections and correlation with the deep-sea $\delta^{18}\text{O}$ record. *Paleoceanography* **17**, 5–1 (2002).
26. Sun, Y. B., Clemens, S. C., An, Z. S. & Yu, Z. W. Astronomical timescale and palaeoclimatic implication of stacked 3.6-Myr monsoon records from the Chinese Loess Plateau. *Quat. Sci. Rev.* **25**, 33–48 (2006).
27. Heller, F. & Liu, T. S. Magnetostratigraphical dating of loess deposits in China. *Nature* **300**, 431–433 (1982).
28. Burbank, D. W. & Li, J. Age and palaeoclimatic significance of the loess of Lanzhou, north China. *Nature* **316**, 429–431 (1985).
29. Kukla, G. et al. Pleistocene climates in China dated by magnetic susceptibility. *Geology* **16**, 811–814 (1988).
30. Sun, D. H., Shaw, J., An, Z. S., Chen, M. Y. & Yue, L. P. Magnetostratigraphy paleoclimatic interpretation of a continuous 7.2 Ma late Cenozoic from the Chinese Loess Plateau. *Geophys. Res. Lett.* **25**, 85–88 (1998).
31. Liu, W. M., Zhang, L. Y. & Sun, J. M. High resolution magnetostratigraphy of the Luochuan loess-paleosol sequence in the central Chinese Loess Plateau. *Chin. J. Geophys.* **53**, 888–894 (2010).
32. Cande, S. C. & Kent, D. V. Revised calibration of the geomagnetic polarity time scales for the late Cretaceous and Cenozoic. *J. Geophys. Res.* **100**, 6093–6095 (1995).
33. Channell, J. E. T., Mazaud, A., Sullivan, P., Turner, S. & Raymo, M. E. Geomagnetic excursions and paleointensities in the 0.9–2.15 Ma interval of the Matuyama Chron at ODP site 983 and 984 (Iceland Basin). *J. Geophys. Res.* **107**, B6 (2002).
34. Liu, Q. S. et al. Magnetostratigraphy of Chinese loess–paleosol sequences. *Earth Sci. Rev.* **150**, 139–167 (2015).
35. Wang, X. S. et al. Remagnetization of quaternary eolian deposits: a case study from SE Chinese Loess Plateau. *Geochem. Geophys. Geosyst.* **6**, Q06H18 (2005).
36. Jin, C. S. & Liu, Q. S. Revisiting the stratigraphic position of the Matuyama–Brunhes geomagnetic polarity boundary in Chinese loess. *Palaeogeogr. Palaeoclimatol. Palaeoecol.* **299**, 309–317 (2011).
37. Nishiizumi, K. et al. Absolute calibration of ^{10}Be AMS standards. *Nucl. Instrum. Methods B* **258**, 403–413 (2007).
38. Nishiizumi, K. Preparation of ^{26}Al AMS standards. *Nucl. Instrum. Methods B* **223**, 388–392 (2004).
39. Lal, D. Cosmic ray labeling of erosion surfaces: in situ nuclide production rates and erosion models. *Earth Planet. Sci. Lett.* **104**, 424–439 (1991).
40. Granger, D. E. et al. New cosmogenic burial ages for Sterkfontein Member 2 Australopithecus and Member 5 Oldowa. *Nature* **522**, 85–88 (2015).
41. Li, J. J. et al. Late Miocene–Quaternary rapid stepwise uplift of the NE Tibetan Plateau and its effects on climatic and environmental changes. *Quat. Res.* **81**, 400–423 (2014).
42. Vandenberghe, J., An, Z. S., Nugteren, G., Lu, H. Y. & Huissteden, K. V. New absolute time scale for the Quaternary climate in the Chinese loess region by grain-size analysis. *Geology* **25**, 35–38 (1997).
43. Hao, Q. Z. et al. Delayed build-up of Arctic ice sheets during 400,000-year minima in insolation variability. *Nature* **490**, 392–396 (2012).
44. Liu, W. G., Yang, H., Sun, Y. B. & Wang, X. L. $\delta^{13}\text{C}$ values of loess total carbonate: a sensitive proxy for Asian summer monsoon in arid northwestern margin of the Chinese Loess Plateau. *Chem. Geol.* **284**, 317–322 (2011).
45. Ding, Z. L. & Yang, S. L. C3/C4 vegetation evolution over the last 7.0 Myr in the Chinese Loess Plateau: evidence from pedogenic carbonate $\delta^{13}\text{C}$. *Palaeogeogr. Palaeoecol. Palaeoclimatol.* **160**, 291–299 (2000).
46. An, Z. S. et al. Multiple expansions of C4 plant biomass in East Asia since 7 Ma coupled with strengthened monsoon circulation. *Geology* **33**, 705–708 (2005).
47. Yang, S. L. et al. Warming-induced northward migration of the East Asian monsoon rain belt from the Last Glacial Maximum to the mid-Holocene. *Proc. Natl Acad. Sci. USA* **112**, 13178–13183 (2015).
48. Rao, Z. G., Zhu, Z. Y., Chen, F. H. & Zhang, J. W. Does $\delta^{13}\text{C}_{\text{carb}}$ of the Chinese loess indicate past C3/C4 abundance? A review of research on stable carbon isotopes of the Chinese loess. *Quat. Sci. Rev.* **25**, 2251–2257 (2006).
49. Li, G. J., Chen, J. & Chen, Y. Primary and secondary carbonate in Chinese loess discriminated by trace element composition. *Geochim. Cosmochim. Acta* **103**, 26–35 (2013).
50. Ning, Y. F., Liu, W. G. & An, Z. S. Variation of soil $\delta^{13}\text{C}$ values in Xifeng loess-paleosol sequence and its paleoenvironmental implication. *Chin. Sci. Bull.* **51**, 1350–1354 (2006).
51. Wang, G. A., Han, J. M. & Liu, T. S. The carbon isotope composition of C3 herbaceous plants in loess area of northern China. *Sci. China Earth Sci.* **46**, 1069–1076 (2003).
52. Rao, Z. G. et al. High-resolution summer precipitation variations in the western Chinese Loess Plateau during the last glacial. *Sci. Rep.* **3**, 2785 (2013).
53. NGRIP members. High-resolution record of Northern Hemisphere climate extending into the last interglacial period. *Nature* **431**, 147–151 (2004).
54. Araya Melo, P. A., Crucifix, M. & Bounceur, N. Global sensitivity analysis of the Indian monsoon during the Pleistocene. *Clim. Past* **11**, 45–61 (2015).
55. Berger, A. & Loutre, M. F. Insolation values for the climate of the last 10 million years. *Quat. Sci. Rev.* **10**, 297–317 (1991).
56. Luethi, D. et al. High-resolution carbon dioxide concentration record 650 000–800 000 years before present. *Nature* **453**, 379–382 (2008).
57. Pertit, J. R. et al. Climate and atmospheric history of the past 420,000 years from the Vostok ice core, Antarctica. *Nature* **399**, 429–436 (1999).
58. Hönisch, B., Hemming, N. G., Archer, D., Siddall, M. & McManus, J. F. Atmospheric carbon dioxide concentration across the mid-Pleistocene transition. *Science* **324**, 1551–1554 (2009).
59. EPICA Community Members. Eight glacial cycles from an Antarctic ice core. *Nature* **365**, 143–147 (2004).
60. Schulz, M. & Stettgen, K. Spectrum: spectral analysis of unevenly spaced palaeoclimatic time series. *Comput. Geosci.* **23**, 929–945 (1997).
61. Torrence, C. & Compo, G. P. A practical guide to wavelet analysis. *Bull. Am. Meteorol. Soc.* **79**, 61–78 (1998).
62. Melice, J. L. & Servain, J. The tropical Atlantic meridional SST gradient index and its relationship with the SOI, NAO and Southern Ocean. *Clim. Dyn.* **20**, 447–464 (2003).
63. Singarayer, J. S. & Valdes, P. J. High-latitude climate sensitivity to ice-sheet forcing over the last 120 kyr. *Quat. Sci. Rev.* **29**, 43–55 (2010).
64. Gordon, C. et al. The simulation of SST, sea ice extents and ocean heat transports in a version of the Hadley Centre coupled model without flux adjustments. *Clim. Dyn.* **16**, 147–168 (2000).
65. Li, Y., Lu, R. Y. & Dong, B. W. The ENSO–Asian monsoon interaction in a coupled ocean–atmosphere GCM. *J. Clim.* **20**, 5164–5177 (2007).
66. Lei, Y. H., Hoskins, B. & Slingo, J. Natural variability of summer rainfall over China in HadCM3. *Clim. Dyn.* **42**, 417–432 (2014).

Acknowledgements

Four anonymous reviewers are acknowledged for their valuable suggestions. We thank S. Spassov and H. Ao for discussing the paleomagnetic results; and L. He, F. Guo, Y. Yan, L. Ma, X. Liu, Y. Cao, X. Li, H. Wang and M. Zhao for field and laboratory assistants. This work was supported by grants from the Ministry of Science and Technology of China (No. 2016YFA0601902), the Chinese Academy of Sciences (No. 132B61KYSB20170005), the National Science Foundation of China (Nos. 41472163, 41525008, and 41572164), and the Fonds de la Recherche Scientifique-FNRS (grant MIS F.4529.18) to Q.Y. and M.C.

Author contributions

Y.S. and Z.A. designed the study and performed the fieldwork. Q.Y., M.C., P.A.-M. and A.B. conducted the sensitivity experiments and analyzed the modeling results. Y.S., L.L., H.C. and Y.L. participated in loess drilling and sampling. S.C. and W.L. contributed to carbonate isotope analysis. Z.A., X.Q., Q.L. and H.Z. analyzed the paleomagnetic data. L.Z., G.D., M.L. and W.Z. conducted the $^{26}\text{Al}/^{10}\text{Be}$ burial dating. All authors contributed to discussion, interpretation of the results, and writing of the manuscript.

Additional information

Supplementary Information accompanies this paper at <https://doi.org/10.1038/s41467-018-08257-9>.

Competing interests: The authors declare no competing interests.

Reprints and permission information is available online at <http://npg.nature.com/reprintsandpermissions/>

Journal peer review information: *Nature Communications* thanks the anonymous reviewers for their contribution to the peer review of this work

Publisher's note: Springer Nature remains neutral with regard to jurisdictional claims in published maps and institutional affiliations.



Open Access This article is licensed under a Creative Commons Attribution 4.0 International License, which permits use, sharing, adaptation, distribution and reproduction in any medium or format, as long as you give appropriate credit to the original author(s) and the source, provide a link to the Creative Commons license, and indicate if changes were made. The images or other third party material in this article are included in the article's Creative Commons license, unless indicated otherwise in a credit line to the material. If material is not included in the article's Creative Commons license and your intended use is not permitted by statutory regulation or exceeds the permitted use, you will need to obtain permission directly from the copyright holder. To view a copy of this license, visit <http://creativecommons.org/licenses/by/4.0/>.

© The Author(s) 2019